Spin-Nematic Vortex States in Cold Atoms

Li Chen [1,2] Yunbo Zhang,[3,*] and Han Pu[4,†]

[1]*Institute of Theoretical Physics and State Key Laboratory of Quantum Optics and Quantum Optics Devices,*
Shanxi University, Taiyuan 030006, China
[2]*Institute for Advanced Study, Tsinghua University, Beijing 100084, China*
[3]*Key Laboratory of Optical Field Manipulation of Zhejiang Province*
and Physics Department of Zhejiang Sci-Tech University, Hangzhou 310018, China
[4]*Department of Physics and Astronomy, and Rice Center for Quantum Materials, Rice University, Houston, Texas 77005, USA*

The (pseudo)spin degrees of freedom greatly enriches the physics of cold atoms. This is particularly so for systems with high spins (i.e., spin quantum number larger than $1/2$). For example, one can construct not only the rank-1 spin vector, but also the rank-2 spin tensor in high spin systems. Here we propose a simple scheme to couple the spin tensor and the center-of-mass orbital angular momentum in a spin-1 cold atom system and show that this leads to a new quantum phase of the matter: the spin-nematic vortex state that features vorticity in an SU(2) spin-nematic tensor subspace. Under proper conditions, such states are characterized by quantized topological numbers. Our work opens up new avenues of research in topological quantum matter with high spins.

Introduction.—Cold atoms are well known to provide an ideal platform for quantum simulation [1]. As a quantum simulator, cold atoms can not only simulate important toy models arising from other subfields of physics, but also offer opportunities to construct new models that take advantages of their unique properties. One particular example is synthetic spin-orbit coupling (SOC) generated either by Raman laser coupling [2–5] or by periodic modulation [6–8]; due to the flexibility of tailoring laser configuration or Floquet engineering, novel types of SOC not naturally occur in other systems can be realized. Another unique property of the atom is that the number of internal states (i.e., the spin) involved can be tuned to some extent, which makes possible the exploration of intriguing physics of high spins [9].

Combining SOC and high spin, SOC in cold atoms with high spins has received much attention in recent years. Raman laser induced SOC in spin-1 condensate [10] was realized by Spielman and co-workers [11], where various phase transitions and the associated quantum tricritical point have been identified. Very recently, interesting phenomena have been explored in a novel type of coupling between the center-of-mass orbital angular momentum (OAM) and the spin vector in spin-1 condensates [12–14] where topological spin vortices, as well as the Hess-Fairback effect, have been observed.

Nevertheless, previous works, including the studies mentioned above, predominantly focus on the textures of the spin operators but few on those of the nematic tensors [9,15,16]. The nematicities, which serve as fundamental quantities in high spin quantum systems, have proved to be of wide usage in distinguishing different phases [9,16] or generating topological structures [9,17,18]. In the current work, we propose to synthesize the coupling between the OAM and the spin-nematic tensor in a spin-1 condensate and show that this coupling leads to a novel vortex state in a special SU(2) subspace spanned by a combination of spin and nematic operators. We call such states, which have never been studied before, the spin-nematic vortex state.

Spin nematic and OAM coupling.—Our proposal builds upon previous studies on coupling spin and OAM [12] and on coupling spin tensor and linear momentum [19] in cold atoms. Specifically, we consider a spin-1 Bose-Einstein condensate (BEC) confined in a three-dimensional harmonic trap with cylindrical symmetry, as is schematically shown in Fig. 1, where the three spin states with magnetic quantum
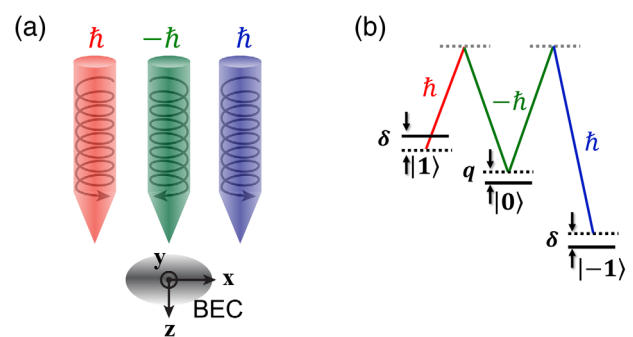

FIG. 1. (a) Schematic of the system. The three laser beams create a pair of Raman transitions that couple the atomic spin nematic tensor and its OAM. (b) Atomic level structure.

number $m_F = 1$, 0, and -1 are Raman coupled by three copropagating Laguerre-Gaussian beams along the z axis. Two of the laser beams carry OAM $L_z = \hbar$ and the third beam has $L_z = -\hbar$. The single-particle Hamiltonian can be written in the cylindrical coordinates (r, ϕ, z) as (taking $\hbar = m = \omega = 1$ with m the atomic mass and ω the transverse trap frequency) [20]

$$H_0 = -\frac{1}{2}\nabla^2 + \frac{1}{2}r^2 + \frac{1}{2}\gamma^2 z^2 + \delta S_z + q S_z^2$$
$$+ i\sqrt{2}\Omega_R(r)(e^{2i\phi}|z\rangle\langle y| - e^{-2i\phi}|y\rangle\langle z|), \quad (1)$$

where $\mathbf{S} = \{S_x, S_y, S_z\}$ are the spin operators, $\gamma = \omega_z/\omega$ the aspect ratio between the longitudinal and the transverse confinement, δ the two-photon Raman detuning which we take to be zero corresponding to the case of two-photon resonance, q the effective quadratic Zeeman energy, $\Omega_R(r) = 2\Omega_0(r/w)^2 e^{-2r^2/w^2}$ the r-dependent Raman coupling strength with Ω_0 characterizing the Raman beam intensity, and w the beam width. In Eq. (1), instead of the bare spin states $|m_F = +1\rangle$, $|0\rangle$, and $|-1\rangle$, we have used the Cartesian polar states $|\mu\rangle$ with $\mu = x$, y, and z, which are defined as the eigenstates to spin operator S_μ with zero eigenvalue, i.e., $S_\mu|\mu\rangle = 0$. In terms of the bare spin states (i.e., eigenstates of S_z), we have $|x\rangle = 1/\sqrt{2}(|-1\rangle - |1\rangle)$, $|y\rangle = i/\sqrt{2}(|-1\rangle + |1\rangle)$, and $|z\rangle = |0\rangle$ [26]. Furthermore, since the Raman induced coupling [last term in Eq. (1)] is only in the transverse r-ϕ plane, we can take our computation in the transverse plane [20]. This effective reduction of spatial dimension allows us to significantly increase our computation efficiency without losing any essential physics.

The coupling between nematic tensor and OAM in H_0 can be more clearly seen when we carry out a gauge rotation $U = \exp(2i\phi S_z^2)$. The new single-particle Hamiltonian $\tilde{H}_0 = U H_0 U^\dagger$ in the rotating frame is given by

$$\tilde{H}_0 = \frac{(i\nabla - \mathbf{A})^2}{2} + \frac{r^2}{2} + q S_z^2 + \sqrt{2}\Omega_R S_x$$
$$= -\frac{\nabla^2}{2} - \frac{2(L_z - S_z^2)S_z^2}{r^2} + \frac{r^2}{2} + q S_z^2 + \sqrt{2}\Omega_R S_x, \quad (2)$$

where $\mathbf{A} = -iU^\dagger\nabla U = 2S_z^2 \hat{e}_\phi/r$ is the synthetic gauge field on the azimuthal direction $\hat{e}_\phi$. In Eq. (2), one can clearly see the spin-nematic-OAM coupling term $\sim L_z S_z^2$ which couples the atomic quasi-OAM $L_z = -i\partial_\phi$ with one of the irreducible nematic tensors $N_{zz} = S_z^2 - 2/3$. It will play a crucial role in inducing various spin-nematic vortex states.

Single-particle properties.—We investigate the spectrum and the eigenstates of $\tilde{H}_0$. First, we realize that L_z is conserved as $[L_z, \tilde{H}_0] = 0$. Furthermore, both L_z and $\tilde{H}_0$ commute with the spin-parity operator,

$$P = |+1\rangle\langle -1| + |-1\rangle\langle +1| + |0\rangle\langle 0|, \quad (3)$$
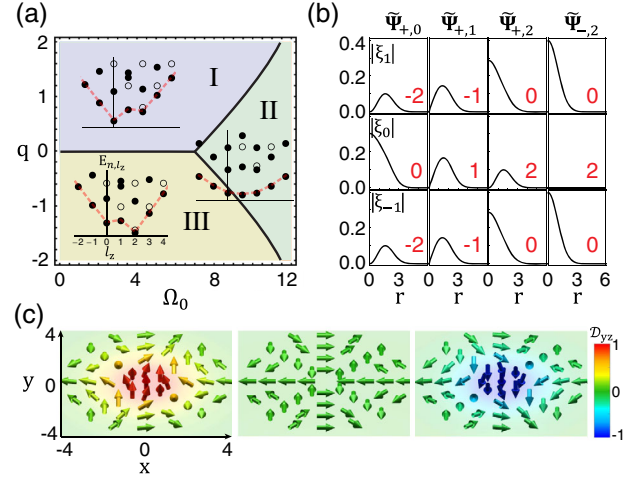

FIG. 2. (a) Single-particle phase diagram with solid lines indicating first-order phase transitions. Insets: Typical dispersion spectra at $(\Omega_0 = 4, q = 0.5)$, $(10,0)$, and $(4, -0.5)$ in three parametric regimes I, II, and III. Solid dots and hollow circles denote the states with even and odd parity, respectively. (b) Spinor wave functions of typical lower-lying eigenstates $\tilde{\Psi}_{P=+,l_z=0,1,2}$ and $\tilde{\Psi}_{P=-,l_z=2}$. Red numbers display the mechanical OAM on each spin component in the lab frame. (c) Typical spin-nematic textures for phase I, II and III (from left to right). Arrows represent the spin-nematic vector $\mathcal{Q} = \{S_x, 2N_{yz}, \mathcal{D}_{yz}\}$, and the arrow color indicates the strength of $\mathcal{D}_{yz}$.

which satisfies $P^2 = 1$. P carries a pair of eigenvalues $P = \pm 1$ distinguishing spin parity of the eigenstates. In particular, the states with even parity ($P = +$) possess the same phase on the ± 1 spin components, whereas those with odd parity ($P = -$) have a phase difference of π on the ± 1 components. It is straightforward to see that the Cartesian state $|x\rangle$ has odd spin parity, while $|y\rangle$ and $|z\rangle$ possess even spin parity. The conservation of L_z ensures the quasi-OAM l_z to be a good quantum number in the rotating frame, and hence the energy eigenstates can be labeled using P and l_z as $\tilde{\Psi}_{P=\pm,l_z} = e^{il_z\phi}\boldsymbol{\xi}_\pm(r) = e^{il_z\phi}[\xi_1(r), \xi_0(r), \xi_{-1}(r)]^T$. The spinor wave function $\boldsymbol{\xi}_\pm(r)$ can be expanded in the Cartesian basis as

$$\boldsymbol{\xi}_+ = \sqrt{\rho(r)}[i\cos\Theta(r)|y\rangle + \sin\Theta(r)|z\rangle],$$
$$\boldsymbol{\xi}_- = \sqrt{\rho(r)}|x\rangle, \quad (4)$$

where $\rho(r) = |\tilde{\Psi}(r)|^2$ is the total particle density and $\Theta(r)$ characterizes the r-dependent superposition weight.

We numerically solve the Schrödinger equation to obtain the energy spectrum and the eigenstates. Figure 2(a) displays the single-particle ground-state phase diagram in the parameter space spanned by Ω_0 and q. Three phases, I, II, and III, can be identified. The ground states in all three phases have even spin parity, while their quasi-OAM quantum numbers l_z are 0, 1, and 2, respectively. All the

phase transitions in the diagram Fig. 2(a) are of first order since, across the phase boundary, the first-order derivative of the ground-state energy with respect to Ω_0 or q exhibits discontinuity [20]. In each phase, we show typical energy spectrum as the inset in Fig. 2(a), where the solid dots and hollow circles distinguish the even and odd spin-parity states. In Fig. 2(b), we plot the magnitude of the wave function for each bare spin component $|\xi_{0,\pm1}|$. The first three columns represent the ground state in each phase, and the last column corresponds to an odd spin-parity state $\tilde{\Psi}_{-,2}$ in phase III that lies very close to the ground state. This state will be important in our later discussion on the many-body effects in a weakly interacting condensate.

The case with vanishing quadratic Zeeman term (i.e., $q = 0$) deserves some special attention. Under this situation, the single-particle spectrum of the even-parity states is symmetric about $l_z = 1$ [20]. For Ω_0 smaller than a critical value $\Omega_c \approx 7$, the line $q = 0$ represents the boundary between phases I and III [see Fig. 2(a)], on which the states $\tilde{\Psi}_{+,l_z}$ with $l_z = 0$ and 2 are degenerate. When $\Omega_0 > \Omega_c$, we enter into phase II with $l_z = 1$. Since the term $(L_z - S_z^2)S_z^2$ in Hamiltonian (2) vanishes for $l_z = 1$ due to $S_z^2 = S_z^4$, S_x is now a conserved quantity. As a result, the spinor wave function $\boldsymbol{\xi}_+$ becomes an eigenstate of S_x featuring $\Theta = \pi/4$.

Spin-nematic vortices.—In the lab frame, different spin components of the single-particle states carry different mechanical OAM as is indicated by the numbers in the subplots of Fig. 2(b). For the spin-0 component, this is simply the quasi-OAM quantum number l_z, whereas for the spin-(±1) component, it is $l_z - 2$. The transformation between the wave function in the lab frame $\boldsymbol{\Psi}$ and that in the rotating frame $\tilde{\boldsymbol{\Psi}}$ is given by $\boldsymbol{\Psi} = U^\dagger \tilde{\boldsymbol{\Psi}}$, which explicitly leads to

$$\boldsymbol{\Psi}_{+,l_z} = \sqrt{\rho(r)}e^{il_z\phi}[ie^{-2i\phi}\cos\Theta(r)|y\rangle + \sin\Theta(r)|z\rangle],$$
$$\boldsymbol{\Psi}_{-,l_z} = \sqrt{\rho(r)}e^{i(l_z-2)\phi}|x\rangle. \tag{5}$$

Clearly, the ground state of phase II, represented by $\boldsymbol{\Psi}_{+,l_z=1}$, is a singular vortex as each of its bare spin components carry a finite vorticity and hence the total density vanishes at $r = 0$, while those in phases I and III, represented by $\boldsymbol{\Psi}_{+,l_z=0,2}$, are coreless vortices that contain at least one spin component with no vorticity with finite density at $r = 0$.

We investigate the spin and nematic textures by calculating the normalized spin density,

$$\mathcal{S}_\mu = \frac{\boldsymbol{\Psi}^\dagger S_\mu \boldsymbol{\Psi}}{\rho(r)}, \tag{6}$$

and the normalized nematic density,

$$\mathcal{N}_{\mu\nu} = \frac{\boldsymbol{\Psi}^\dagger N_{\mu\nu}\boldsymbol{\Psi}}{\rho(r)}, \tag{7}$$

where $N_{\mu\nu} = \frac{1}{2}(S_\mu S_\nu + S_\nu S_\mu) - \frac{2}{3}\delta_{\mu\nu}$ are the symmetrized SU(3) nematic tensors with nine components by taking $\mu, \nu = x, y, z$ [9,15,16]. Diagonalizing the nematic density matrix $\mathcal{N}$ results in three eigenvalues $\lambda_{1,2,3}$ characterizing the alignment axis of nematic orders. A uniaxial nematic state is characterized by $\lambda_1 \neq \lambda_2 = \lambda_3$, while for a biaxial nematic state, none of these eigenvalues are equal. We remark that the Cartesian states are closely related to the SU(3) operators, which greatly facilitates the calculation of $\mathcal{S}$ and $\mathcal{N}$ [20].

Now we discuss the four low-energy states $\boldsymbol{\Psi}_{+,l_z=0,1,2}$ and $\boldsymbol{\Psi}_{-,l_z=2}$ represented in Fig. 2(b). The odd-parity state $\boldsymbol{\Psi}_{-,2}$ is topologically trivial, since it is simply a polar state with vanishing spin density, and a fixed uniaxial direction along N_{xx}. For the even-parity states $\boldsymbol{\Psi}_{+,l_z=0,1,2}$ which represent the ground state in the three phases, we have

$$\boldsymbol{\mathcal{S}} = \{-\cos(2\phi)\sin(2\Theta), 0, 0\},$$

$$\mathcal{N} = \begin{bmatrix} \frac{1}{3} & 0 & 0 \\ 0 & -\frac{1}{6}(1+3\cos2\Theta) & -\frac{1}{2}\sin(2\Theta)\sin(2\phi) \\ 0 & -\frac{1}{2}\sin(2\Theta)\sin(2\phi) & -\frac{1}{6}(1-3\cos2\Theta) \end{bmatrix}, \tag{8}$$

where the spin vector $\boldsymbol{\mathcal{S}}$ is polarized along S_x. The eigenvalues of the nematic matrix $\mathcal{N}$ can be obtained as $\lambda_1 = 1/3$, $\lambda_{2,3} = -1/6[1 \pm 3\sqrt{1 - \sin^2(2\Theta)\cos^2(2\phi)}]$, indicating that all three states are biaxial nematic states. Furthermore, the spin and nematic densities in Eq. (8) are not independent, and satisfy [15]

$$\frac{1}{2}|\boldsymbol{\mathcal{S}}^2| + \text{Tr}[\mathcal{N}^2] = \frac{2}{3}. \tag{9}$$

Substituting Eq. (8) into Eq. (9), one immediately obtains a relation

$$\mathcal{S}_x^2 + \mathcal{D}_{yz}^2 + (2\mathcal{N}_{yz})^2 = 1, \tag{10}$$

where $\mathcal{D}_{yz} = \mathcal{N}_{yy} - \mathcal{N}_{zz} = -\cos(2\Theta)$. This relation motivates the construction of the following spin-nematic vector,

$$\boldsymbol{\mathcal{Q}} = \{\mathcal{S}_x, 2\mathcal{N}_{yz}, \mathcal{D}_{yz}\}, \tag{11}$$

which forms vector space lying on a unit Bloch sphere. In fact, the vector $\boldsymbol{\mathcal{Q}}$ is defined on an SU(2) group generated by $\mathbf{Q} = \{S_x, 2N_{yz}, D_{yz} = N_{yy} - N_{zz}\}$. Mathematically, the group $\mathbf{Q}$ is a type-2 subgroup of the SU(3) Lie group with the structure constant being equal to 2 [20,27], i.e., $[2N_{yz}, S_x] = 2iD_{yz}$.

In Fig. 2(c), we display the textures of the spin-nematic vector $\boldsymbol{\mathcal{Q}}$ for the ground states of the three phases

$\Psi_{+,l_z=0,1,2}$. One can clearly see that the transverse components of $\mathcal{Q}$ for all three states form a vortex pattern, hence the name spin-nematic vortex states.

We now investigate the topological properties of the spin-nematic vortex states. Let us first focus on the $q = 0$ case. The ground state in phase II is a singular vortex state $\Psi_{+,l_z=1}$ satisfying $\Theta = \pi/4$, as mentioned before. Hence $\mathcal{Q}$ is a planar vector that lies on the equator of the Bloch sphere since its z component vanishes, i.e., $\mathcal{D}_{yz} = -\cos(2\Theta) = 0$. This allows us to depict the singular vortex $\Psi_{+,l_z=1}$ by the winding number, which counts the winding times of $\mathcal{Q}$ as one walks along a closed loop in the x-y plane. Apparently, the winding number of the singular vortex $\Psi_{+,l_z=1}$ equals to -2 if the loop encloses the vortex core (at the origin $x = y = 0$), and equals to 0 otherwise. For the two coreless states $\Psi_{+,l_z=0,2}$ of phases I and III, the spin-nematic vector $\mathcal{Q}$ is defined on the whole Bloch sphere. However, we have the boundary condition $\Theta(r \to \infty) = \pi/4$, which can be clearly observed as the contribution of term $(L_z - S_z^2)S_z^2/r^2$ in Hamiltonian (2) diminishes as $r \to \infty$. Consequently, each state ($\Psi_{+,l_z=0}$ or $\Psi_{+,l_z=2}$) covers one half of the Bloch sphere, and their topological number can thus be characterized by the skyrmion number [28] defined as

$$\mathcal{W} = \frac{1}{4\pi} \iint d^2r \, \mathcal{Q} \cdot (\partial_x \mathcal{Q} \times \partial_y \mathcal{Q}), \qquad (12)$$

which turns out to be ∓ 1 for states $\Psi_{+,l_z=0,2}$, respectively [29]. Note that the coreless spin-nematic vortices defined in the type-2 subspace $\mathbf{Q}$ here are analogous to the Mermin-Ho vortex [30–32] defined in the type-1 subspace $\mathbf{S} = \{S_x, S_y, S_z\}$. However, the two are not mathematically equivalent since the subspaces $\mathbf{S}$ and $\mathbf{Q}$ cannot be transformed into each other by SU(3) rotations [27]. We also note that these topological numbers are not well defined at finite q. For example, at finite q, the singular vortex can no longer be described by the winding number since $\mathbf{Q}$ is no longer restricted in the $S_x - 2N_{yz}$ plane, and the skyrmion numbers of the other two coreless vortices are also in general not quantized to be integers.

Many-body effects.—Next, we consider a weakly interacting condensate and discuss the effects of the interactions under the framework of the mean-field theory. In the lab frame, the interacting Hamiltonian of the spin-1 condensate is in the well-known form of [9,33]

$$H_{\text{int}} = \frac{1}{2} \int d^2r \rho^2(\mathbf{r})[c_0 + c_2 \mathbf{S}^2(\mathbf{r})], \qquad (13)$$

where c_0 and c_2 denote the strength of the density-density and the spin-exchange interactions, respectively. We implement two different methods to obtain the mean-field ground states—the variational method and the numerical method by solving 3D Gross-Pitaevskii equations [20], and the
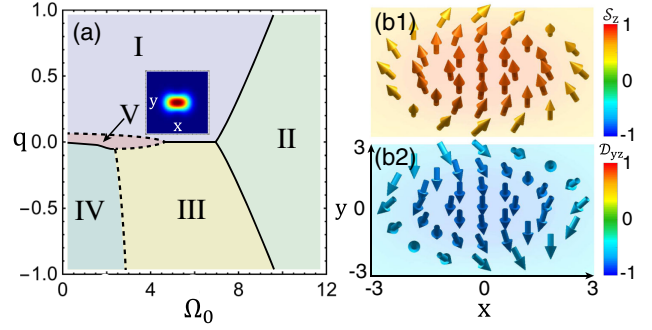

FIG. 3. (a) Many-body phase diagram, where the solid and the dashed lines indicate the first- and the second-order phase transitions, respectively. Insets: Total density profile $\rho(r)$ of phase V. Panels (b1) and (b2) display the typical spin texture $\mathbf{S} = \{\mathcal{S}_x, \mathcal{S}_y, \mathcal{S}_z\}$ and spin-nematic texture $\mathcal{Q} = \{\mathcal{S}_x, 2\mathcal{N}_{yz}, \mathcal{D}_{yz}\}$ of phase IV, respectively. The arrow color in (b1) and (b2) indicates the z components of the spin density $\mathbf{S}$ and spin-nematic density $\mathcal{Q}$, respectively.

results turn out to be in excellent agreement. For the variational method, we assume the condensate wave function is a linear combination of the four lower-lying single-particle states shown in Fig. 2(b):

$$\tilde{\Psi} = D_0 \tilde{\Psi}_{+,0} + D_1 \tilde{\Psi}_{+,1} + D_+ \tilde{\Psi}_{+,2} + D_- \tilde{\Psi}_{-,2}, \qquad (14)$$

where $D_{j=0,1,+,-} = |D_j|e^{i\theta_j}$ are variational amplitudes satisfying $\sum_j |D_j|^2 = 1$, with θ_j being the phase angle of D_j. We obtain the ground states by minimizing the total energy functional with respect to D_j. Here, we consider a weak ferromagnetic spin-exchange interaction by taking $c_0 = 1$ and $c_2 = -0.1c_0$, and then map out the ground-state phase diagram as is displayed in Fig. 3(a).

The main structures of the many-body phase diagram Fig. 3(a) are consistent with that of the single-particle phase diagram Fig. 2(a). In Fig. 3(a), the three phases I, II, and III are very similar to the corresponding single-particle ones in diagram Fig. 2(a) with $|D_{j=0,1,+}| = 1$ in ansatz (14), respectively, and the phase transitions among them are all of first order (solid lines). There are, however, two new many-body phases labeled as IV and V that have no counterparts in the single-particle phase diagram, and the phase transitions related to them can be either first (solid lines) or second order (dashed lines), as determined by whether the first- or second-order derivatives of the ground state energy with respect to the parameters (Ω or q) exhibit discontinuity or not [20].

These two new phases, IV and V, spontaneously break the spin parity and the rotation symmetry, respectively. Specifically, the wave function of phase IV is a superposition of states $\tilde{\Psi}_{\pm,2}$ with variational amplitudes satisfying $|D_\pm| \neq 0$ and $\theta_+ - \theta_- = 0$ or π (mod[2π]). Thus, it keeps the rotational symmetry but breaks the spin-parity symmetry. Interestingly, this state exhibits vorticity in both

the spin and the spin-nematic subspaces **S** and **Q** simultaneously, as are shown in Figs. 3(b1) and 3(b2) respectively. The breaking of the spin-parity symmetry is manifested in the fact that S_z is finite, i.e., unequal occupation on the bare spin-(±1) components.

The wave function of phase V is a superposition of states $\tilde{\Psi}_{+,0}$ and $\tilde{\Psi}_{+,2}$ with $|D_{0,+}| \neq 0$. Thus, this state maintains the spin-parity symmetry, but breaks the rotational symmetry, which leads to an interesting angular striped phase [34,35]. We show the total density profile $\rho(r)$ of phase V as an inset in Fig. 3(a), where the lack of the rotational symmetry is obvious.

Experimental observation.—Finally, let us briefly discuss the experimental detection of the spin-nematic vortex states, which can be performed either directly or indirectly. The indirect observation is to detect such features of the wave functions $\Psi_{+,l_z=0,1,2}$ [presented in Fig. 2(b)] as the core structures or the mechanical-OAM numbers. Specifically, the core structure can be obtained by the spin-selected absorption imaging; the mechanical-OAM quantum numbers can be deduced from the interference pattern after different spin components are mixed with each other by a radio frequency $\pi/2$ pulse [13,14]. In contrast, the direct observation is to detect the spin-nematic textures $\mathcal{Q}$ directly. Since the direct observation of the spin texture $\mathcal{S}$ was realized via spin-sensitive dispersive imaging a few years ago [36,37], this technique can be easily generalized to measure $\mathcal{Q}$ as the nematic operators $2N_{yz}$ and D_{yz} are rotated into the measurable direction S_x. Practically, this rotation can be achieved by pulsing a quadratic Zeeman magnetic field which lets **Q** evolve under the government of $\sim S_z^2$ [38], or more feasibly, introducing an additional far off-resonant microwave on certain Zeeman level [39].

Summary.—We have proposed a scheme to couple the atomic OAM and the nematic tensor in a spin-1 cold atomic system. The ground state exhibits vorticity in a special spin-nematic subspace. Under zero quadratic field, the spin-nematic vortices can be characterized by quantized topological numbers. These features survive in the presence of weak interaction. However, the interaction may induce spontaneous symmetry breakings, and leads to a rich many-body phase diagram. Considering the spin-OAM coupling has been realized by two experimental groups very recently [13,14,40], we expect this work to stimulate more investigations on the spin-OAM coupled quantum gases with higher spins and nematic orders.

*ybzhang@zstu.edu.cn
†hpu@rice.edu

[1] I. Bloch, J. Dalibard, and S. Nascimbène, Nat. Phys. **8**, 267 (2012).

[2] V. Galitski and I. B. Spielman, Nature (London) **494**, 49 (2013).

[3] N. Goldman, G. Juzeliūnas, P. Öhberg, and I. B. Spielman, Rep. Prog. Phys. **77**, 126401 (2014).

[4] H. Zhai, Rep. Prog. Phys. **78**, 026001 (2015).

[5] *Synthetic Spin-Orbit Coupling in Cold Atoms*, edited by W. Zhang, W. Yi, and C. A. R. S. Melo (World Scientific, Singapore, 2018).

[6] C. Chin, Nat. Phys. **15**, 1106 (2019).

[7] F. Görg, K. Sandholzer, J. Minguzzi, R. Desbuquois, M. Messer, T. Esslinge, and M. Aidelsburger, Nat. Phys. **15**, 1161 (2019).

[8] C. Schweizer, F. Grusdt, M. Berngruber, L. Barbiero, E. Demler, N. Goldman, I. Bloch, and M. Aidelsburger, Nat. Phys. **15**, 1168 (2019).

[9] K. Kawaguchi and M. Ueda, Phys. Rep. **520**, 253 (2012).

[10] Z. H. Lan and P. Öhberg, Phys. Rev. A **89**, 023630 (2014); S. S. Natu, X. P. Li, and W. S. Cole, *ibid.* **91**, 023608 (2015); K. Sun, C. Qu, Y. Xu, Y. Zhang, and C. Zhang, *ibid.* **93**, 023615 (2016); Z.-Q. Yu, *ibid.* **93**, 033648 (2016); G. I. Martone, F. V. Pepe, P. Facchi, S. Pascazio, and S. Stringari, Phys. Rev. Lett. **117**, 125301 (2016).

[11] D. L. Campbell, R. M. Price, A. Putra, A. Valdés-Curiel, D. Trypogeorgos, and I. B. Spielman, Nat. Commun. **7**, 10897 (2016).

[12] L. Chen, H. Pu, and Y. Zhang, Phys. Rev. A **93**, 013629 (2016).

[13] H.-R. Chen, K.-Y. Lin, P.-K. Chen, N.-C. Chiu, J.-B. Wang, C.-A. Chen, P.-P. Huang, S.-K. Yip, Y. Kawaguchi, and Y.-J. Lin, Phys. Rev. Lett. **121**, 113204 (2018).

[14] P.-K. Chen, L.-R. Liu, M.-J. Tsai, N.-C. Chiu, Y. Kawaguchi, S.-K. Yip, M.-S. Chang, and Y.-J. Lin, Phys. Rev. Lett. **121**, 250401 (2018).

[15] E. J. Mueller, Phys. Rev. A **69**, 033606 (2004).

[16] D. Podolsky and E. Demler, New J. Phys. **7**, 59 (2005).

[17] J. Ruostekoski and J. R. Anglin, Phys. Rev. Lett. **91**, 190402 (2003).

[18] M. Ueda, Rep. Prog. Phys. **77**, 122401 (2014).

[19] X.-W. Luo, K. Sun, and C. Zhang, Phys. Rev. Lett. **119**, 193001 (2017).

[20] See Supplemental Material at http://link.aps.org/supplemental/10.1103/PhysRevLett.125.195303 for more information on the derivation of H_0, the symmetry of the single-particle spectrum at $q = 0$, the SU(3) algebras and calculation details of the spin and nematic orders, phase diagrams and quantum phase transitions, and the calculation details of the 3D Gross-Pitaevskii equations, which includes Refs. [21–25].

[21] F. Schmidt, D. Mayer, M. Hohmann, T. Lausch, F. Kindermann, and A. Widera, Phys. Rev. A **93**, 022507 (2016).

[22] Y.-J. Lin, K. Jiménez-García, and I. B. Spielman, Nature (London) **471**, 83 (2011).

[23] J. Stenger, S. Inouye, D. M. Stamper-Kurn, H.-J. Miesner, A. P. Chikkatur, and W. Ketterle, Nature (London) **396**, 345 (1998).

[24] C. D. Hamley, E. M. Bookjans, G. Behin-Aein, P. Ahmadi, and M. S. Chapman, Phys. Rev. A **79**, 023401 (2009).

[25] W. Bao and Y. Cai, Kinet. Relat. Models **6**, 1 (2013).

[26] T. Ohmi and K. Machida, J. Phys. Soc. Jpn. **67**, 1822 (1998).

[27] E. Yukawa, M. Ueda, and K. Nemoto, Phys. Rev. A **88**, 033629 (2013).

[28] N. Nagaosa and Y. Tokura, Nat. Nanotechnol. **8**, 899 (2013).

[29] At $q = 0$, the two coreless vortex states $\Psi_{+,l_z=0,2}$ are energetically degenerate in the single-particle level. Hence any linear superposition of these two states remains as an eigenstate of the single-particle Hamiltonian. These two states have well-defined winding numbers, but not their superpositions. However, this issue can be avoided as a weak density-density interaction is included into the system. Since these two states feature identical total density profile, the presence of the density-density interaction (c_0 term) does not break their symmetry. However, any superposition of these two states would lead to spatial stripes with higher peak densities, and hence an excessive interaction energy. Thus the interaction term favors either $\Psi_{+,l_z=0}$ or $\Psi_{+,l_z=2}$, but not their superposition. For details, see Supplemental Material [20].

[30] N. D. Mermin and Tin-Lun Ho, Phys. Rev. Lett. **36**, 594 (1976).

[31] N. D. Mermin, Rev. Mod. Phys. **51**, 591 (1979).

[32] H. Makela, Y. Zhang, and K.-A. Suominen, J. Phys. A **36**, 8555 (2003).

[33] D. M. Stamper-Kurn and M. Ueda, Rev. Mod. Phys. **85**, 1191 (2013).

[34] J.-R. Li, J. Lee, W. Huang, S. Burchesky, B. Shteynas, F. C. Top, A. O. Jamison, and W. Ketterle, Nature (London) **543**, 91 (2017).

[35] J. Lonard, A. Morales, P. Zupancic, T. Esslinger, and Tobias Donner, Nature (London) **543**, 87 (2017).

[36] J. M. Higbie, L. E. Sadler, S. Inouye, A. P. Chikkatur, S. R. Leslie, K. L. Moore, V. Savalli, and D. M. Stamper-Kurn, Phys. Rev. Lett. **95**, 050401 (2005).

[37] L. Sadler, J. Higbie, S. R. Leslie, M. Vengalattore, and D. M. Stamper-Kurn, Nature (London) **443**, 312 (2006).

[38] M.-S. Chang, Q. Qin, W. Zhang, and M. S. Chapman, Nat. Phys. **1**, 111 (2005).

[39] C. D. Hamley, C. S. Gerving, T. M. Hoang, E. M. Bookjans, and M. S. Chapman, Nat. Phys. **8**, 305 (2012).

[40] D. Zhang, T. Gao, P. Zou, L. Kong, R. Li, X. Shen, X.-L. Chen, S.-G. Peng, M. Zhan, H. Pu, and K. Jiang, Phys. Rev. Lett. **122**, 110402 (2019).